

In₂O₃-Based Transparent Conducting Oxide Films with High Electron Mobility Fabricated at Low Process Temperatures

Takashi Koida,* Yuko Ueno, and Hajime Shibata

The emerging technological demands for high-efficiency solar cells and flexible optoelectronic devices have stimulated research on transparent conducting oxide (TCO) electrodes. High-mobility TCOs are needed to achieve high conductivity with improved visible and near-infrared transparency; however, the fabrication of TCO films on heat-sensitive layers or substrates is constrained by the trade-off between fabrication temperatures and TCO properties. Historically, Sn-doped indium oxide and amorphous In–Zn–O have been used as standard TCOs to achieve high mobility using low fabrication temperatures. However, two polycrystalline In₂O₃ films with significantly higher mobilities have recently been reported: i) polycrystalline (*poly*-) In₂O₃ films doped with metal (Ti, Zr, Mo, or W) impurities instead of Sn exhibit mobilities greater than $\approx 80 \text{ cm}^2 \text{ V}^{-1} \text{ s}^{-1}$ even when grown at low temperatures and ii) solid-phase crystallized (*spc*-) H-doped In₂O₃ (In₂O₃:H) and In₂O₃:Ce,H films exhibit mobilities greater than $100 \text{ cm}^2 \text{ V}^{-1} \text{ s}^{-1}$ when processed at low temperatures of 150–200 °C. Here, *poly*-In₂O₃, In₂O₃:W, and In₂O₃:Ce films and *spc*-In₂O₃:H, In₂O₃:W,H, and In₂O₃:Ce,H films are fabricated. Comparative studies of these films reveal the effect of the i) metal dopant species; ii) metal and hydrogen codoping; and iii) solid-phase crystallization process on the resultant transport properties.

1. Introduction

Transparent conducting oxide (TCO) films have been widely used as window electrodes in optoelectronic applications such as displays, light-emitting diodes, and solar cells. The continuous development of solar cells (e.g., thin-film Si, chalcopyrite, organic, perovskite, and Si-wafer-based heterojunction solar cells) has stimulated research on TCO films (e.g., In₂O₃,^[1–6] ZnO,^[1,7–10] and SnO₂^[11]). For example, high electron mobility is required for the TCO films used in solar cells because a high-mobility results in a low sheet resistance at a low carrier density, providing high transparency with reduced free-carrier absorption in the visible


and near-infrared regions.^[12–16] Low-temperature growth is also required because of the presence of temperature-sensitive layers in many solar cells (e.g., Si heterojunction,^[17,18] Cu(In,Ga)(Se,S)₂,^[19,20] and perovskite^[21,22] solar cells). Polycrystalline (*poly*-) Sn-doped In₂O₃ (ITO)^[23–25] and amorphous-In₂O₃-based TCOs (e.g., *a*-ITO^[25,26] and *a*-In–Zn–O (*a*-IZO)^[27,28]) have been broadly used to satisfy these requirements. *Poly*-ITO films grown at temperatures below 200–300 °C exhibit a high electron mobility (μ) of $\approx 40 \text{ cm}^2 \text{ V}^{-1} \text{ s}^{-1}$ with a low resistivity (ρ) of $\approx 1 \times 10^{-4} \Omega \text{ cm}$,^[29] whereas *a*-IZO films deposited even at room temperature exhibit a high μ of $\approx 60 \text{ cm}^2 \text{ V}^{-1} \text{ s}^{-1}$ with a relatively low ρ of $\approx 3 \times 10^{-4} \Omega \text{ cm}$.^[30,31]

Recently, two types of In₂O₃ films with higher μ values have been reported. First, *poly*-In₂O₃ films doped with metal (Ti,^[1,32] Zr,^[1,33,34] Mo,^[1,35–39] or W^[5,40]) impurities (In₂O₃:Me) instead of Sn exhibit μ values greater than $\approx 80 \text{ cm}^2 \text{ V}^{-1} \text{ s}^{-1}$ at a carrier density (N) from 1×10^{20} to $3 \times 10^{20} \text{ cm}^{-3}$. These films are normally deposited onto heated substrates using various growth methods (e.g., magnetron sputtering,

pulsed laser deposition, and ion plating with DC arc discharge, known as high-density plasma-enhanced evaporation or reactive plasma deposition (RPD)). Second, solid-phase crystallized (*spc*-) H-doped In₂O₃ (In₂O₃:H) films exhibit μ values greater than $100 \text{ cm}^2 \text{ V}^{-1} \text{ s}^{-1}$ with N values from 1×10^{20} to $2 \times 10^{20} \text{ cm}^{-3}$ at low process temperatures from 150 to 200 °C.^[41] The films are fabricated using a two-step growth process, specifically, the deposition of amorphous or amorphous-rich In₂O₃:H films grown at low temperatures via magnetron sputtering,^[41] RPD,^[42] or atomic layer deposition^[43] and subsequently thermally annealed at a temperature greater than 150 °C. During annealing, solid-phase crystallization occurs and high electron mobility is achieved. Similar properties have also been reported for CeO₂ and hydrogen co-doped In₂O₃ films.^[42] Notably, *spc*-In₂O₃:H films on glass substrates fabricated at low process temperatures (≤ 200 °C) exhibited higher μ values than Me-doped epitaxial films grown at high temperatures (≥ 600 °C) on single-crystalline oxide substrates.^[15,44,45]

The mechanisms responsible for this high electron mobility have been investigated. Analysis of effective mass has been conducted as a function of N for various specimens, including

Dr. T. Koida, Y. Ueno, Dr. H. Shibata
Research Center for Photovoltaics
National Institute of Advanced Industrial Science and Technology
1-1-1 Umezono, Tsukuba 305-8568, Japan
E-mail: t-koida@aist.go.jp

 The ORCID identification number(s) for the author(s) of this article can be found under <https://doi.org/10.1002/pssa.201700506>.

DOI: 10.1002/pssa.201700506

polycrystalline and epitaxial films and bulk single crystals, to determine the curvature of the energy band as a function of the Fermi energy.^[38,40,46–50] High- μ TCO films exhibited an electron effective mass similar to those of conventional *poly*-ITO and *a*-In₂O₃-based TCO films, indicating that high μ is achieved through a larger relaxation time rather than a smaller effective mass.^[47,49] In polycrystalline films, the overall relaxation time is determined by scattering induced by grain boundaries (GBs), stacking faults, dislocations, point defects including neutral and ionized impurities, and phonons.^[51,52] The effect of GB scattering can be evaluated from the ratio between the Hall mobility and the optical mobility: Hall mobilities are affected by GB scattering when electrons transport across GBs, whereas optical mobilities are not affected by GBs because free electrons exist inside grains and because the amplitude of oscillation of an electron under the influence of an electromagnetic field is much smaller than the grain sizes in typical TCO films.^[13] In the *spc*-In₂O₃:H films, the effect of GBs was found to be minor because these films' optical mobilities were comparable to their Hall mobilities.^[47] Furthermore, the effects of dopant species (Me and H) on the grain-barrier height and resulting transport properties in polycrystalline films have also been discussed.^[53] With respect to intragrain properties, suppressed scattering from oxygen interstitials^[36,39,40] originating from the formation of the singly charged donor (e.g., Mo_{In}^{•••}O_i[•], W_{In}^{•••}O_i[•]) and suppressed scattering from defects related to oxygen deficiencies^[34,42,44,54] originating from the introduction of metals with higher bond strength with O than In and Sn in the In₂O₃ host material have been discussed. In In₂O₃:H films, *ab initio* calculations revealed that interstitial H (H_i[•]) and substitutional H (H_O[•]) function as singly charged donors, being energetically more favorable than an oxygen vacancy (V_O^{••}).^[55] Additionally, interstitial hydrogen atoms have been reported to passivate negatively charged acceptor-type cation vacancies.^[56] Experimentally determined N and μ data have been evaluated on the basis of theoretical carrier scattering models and used to determine the doping mechanisms. The Hall mobility values agreed well with the calculated values dominated by singly charged impurities, which suggests that the free carriers were generated by singly charged donors (e.g., Me_{In}[•], H_i[•], H_O[•]) rather than by doubly charged donors (e.g., V_O^{••}) in In₂O₃:Me,^[32,34,44] In₂O₃:H,^[41] and In₂O₃:Ce,H.^[42] However, the degenerately doped TCO films exhibited higher electron mobility with constant N at lower temperatures than at higher temperatures, indicating that the μ values measured at room temperature were limited not only by the ionized impurity scattering but also by phonon scattering.^[34,41] Therefore, the good agreement of the values suggests imperfections of the modeled mobility. An extended model based on scatterings produced by phonon and ionized impurities has also been discussed.^[49] Currently, the model cannot quantitatively explain the experimentally determined high μ values, especially at N values greater than $1 \times 10^{19} \text{ cm}^{-3}$; however, a more in-depth understanding of acoustic deformation potential scattering, polar optical phonon scattering, and ionized impurity scattering in these materials was achieved.^[49,53,57]

In this study, to clarify the commonalities and disparities between the two types of In₂O₃ films with high μ , we fabricated *poly*-In₂O₃, In₂O₃:W, and In₂O₃:Ce films in the as-deposited state and *spc*-In₂O₃:H, In₂O₃:W,H, and In₂O₃:Ce,H films and

evaluated their structural, electrical, and optical properties. All of the films were deposited using an RPD system, and the deposition conditions were fixed as much as possible (except for variables such as the dopant species and concentrations, substrate temperatures, and H₂O vapor pressures during growth) to minimize fluctuations in film properties as a consequence of changes in the experimental conditions. Comparative studies of these films revealed the effect of the i) metal dopant species; ii) metal and hydrogen codoping; and iii) solid-phase crystallization process on the resulting transport properties. Among the fabricated films, the *spc*-In₂O₃:Ce,H exhibited the lowest ρ of $1.81 \times 10^{-4} \Omega \text{ cm}$ with a μ of $154 \text{ cm}^2 \text{ V}^{-1} \text{ s}^{-1}$ and N of $2.24 \times 10^{20} \text{ cm}^{-3}$.

2. Results and Discussion

2.1. Structural Properties

Table 1 summarizes the ratios of metal (W and Ce) to In determined using inductively coupled plasma mass spectrometry (ICP-MS) analysis for the as-deposited In₂O₃:W,H (WO₃: 1 wt.%) and In₂O₃:Ce,H (CeO₂: 1, 2, and 3 wt.%) films without substrate heating. In this analysis, the Cu and Mo impurity contents resulting from the RPD system were also measured to investigate their effect on the films. The Cu, Mo, and Ce (W) concentrations in the In₂O₃:W,H (In₂O₃:Ce,H) film were less than the lower detection limits (0.0036 at.% for Cu/In, 0.0024 at.% for Mo/In, 0.0016 at.% for Ce/In, and 0.0012 at.% for W/In) of the instrument. The W-to-In atomic ratio was 0.39 at.% in the In₂O₃:W,H (WO₃: 1 wt.%) films, and the Ce-to-In ratios were 0.28, 0.96, and 1.3 at.% in the In₂O₃:Ce,H (CeO₂: 1, 2, and 3 wt.%) films, respectively. Herein, we applied the same ratios in the post-annealed films and the films deposited at 200 °C because tungsten oxides and cerium oxides did not effuse from the films during annealing at 250 °C, and the sticking coefficients of W and Ce would not change significantly at a substrate temperature of 200 °C.

Figure 1 plots the H contents in the films as a function of the partial pressure of H₂O ($P_{\text{H}_2\text{O}}$). The H contents systematically increased with increasing $P_{\text{H}_2\text{O}}$ in the films without substrate heating, whereas the values were below 0.5 at.% for the films deposited at 200 °C. The high $P_{\text{H}_2\text{O}}$ of 2×10^{-4} to $3 \times 10^{-4} \text{ Pa}$ before the *poly*-In₂O₃ and In₂O₃:Me depositions originated from the degassing of H₂O vapor from the areas around the heater in the RPD chamber. The large difference in H contents between

Table 1. Atomic ratios of metal (W and Ce) to In determined by ICP-MS analysis for the as-deposited In₂O₃:W,H (WO₃: 1 wt.%) and In₂O₃:Ce,H (CeO₂: 1, 2, and 3 wt.%) films without substrate heating. The detection limits were 0.0012 at.% for W/In and 0.0016 at.% for Ce/In.

	W/In (at.%)	Ce/In (at.%)
In ₂ O ₃ :H,W (WO ₃ : 1 wt.%)	0.39	–
In ₂ O ₃ :H,Ce (CeO ₂ : 1 wt.%)	–	0.28
In ₂ O ₃ :H,Ce (CeO ₂ : 2 wt.%)	–	0.96
In ₂ O ₃ :H,Ce (CeO ₂ : 3 wt.%)	–	1.3

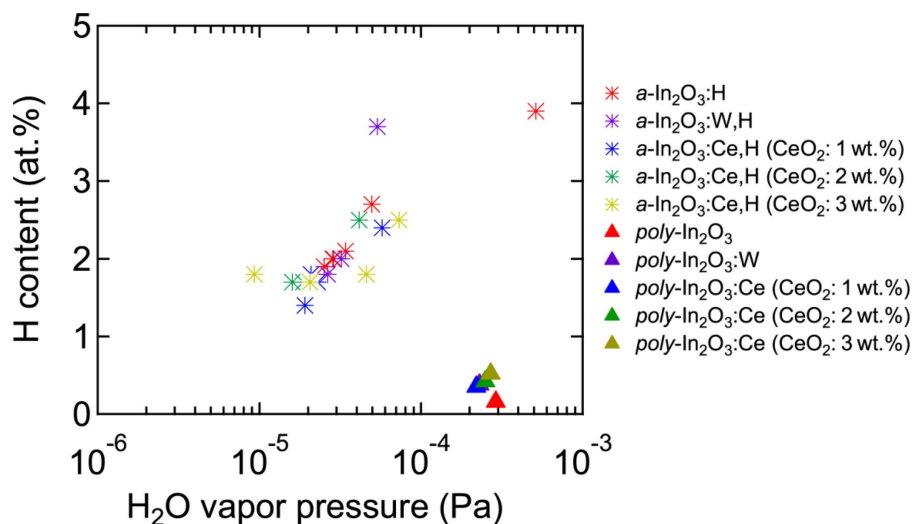


Figure 1. H contents in the *a*-In₂O₃:H, In₂O₃:W,H, and In₂O₃:Ce,H films without substrate heating (<60 °C) and in the *poly*-In₂O₃, In₂O₃:W, and In₂O₃:Ce films deposited at 200 °C.

the films deposited in the absence and presence of heating indicates that the sticking probabilities of H atoms and OH species at the growth surface increased with decreasing deposition temperature. Thermal desorption spectroscopy (TDS) analysis revealed that $\approx 10\%$ of the total H contents in the films deposited without substrate heating effused at temperatures as high as 250 °C (not shown here), which is similar to the case of *a*-In₂O₃:H films fabricated using magnetron sputtering.^[47] Therefore, the H contents in the crystallized films at 250 °C did not substantially decrease compared with those in the as-deposited films.^[41,47] The same result was observed for the In₂O₃ and In₂O₃:Me films; $\approx 9\%$ of the total H contents in the films effused at temperatures as high as 200 °C, the growth temperature of the films, indicating that most of the effusion originated from the bulk of the films and not from adsorbates at the surface exposed to the atmosphere before the TDS characterization.

Figure 2 presents scanning electron microscopy (SEM) images of *poly*-In₂O₃, In₂O₃:W, In₂O₃:Ce (CeO₂: 1 wt.%), and In₂O₃:Ce (CeO₂: 3 wt.%) films deposited at 200 °C and *spc*-In₂O₃:H, In₂O₃:W,H, In₂O₃:Ce,H (CeO₂: 1 wt.%), and In₂O₃:Ce,H (CeO₂: 3 wt.%) films deposited at low and high $P_{\text{H}_2\text{O}}$. All of the *poly*-In₂O₃ and In₂O₃:Me films exhibited grain sizes of ≈ 50 nm. Conversely, all of the as-deposited In₂O₃:H and In₂O₃:Me,H films without substrate heating exhibited featureless structures with smooth surfaces because of the amorphous-phase formation (not shown here). After the post-annealing treatment at 250 °C, the films exhibited large grain structures. The grain size and shape were dependent on $P_{\text{H}_2\text{O}}$ during deposition: the *spc*-In₂O₃:H and In₂O₃:Me,H films with low Me contents deposited at low $P_{\text{H}_2\text{O}}$ exhibited only polygonal structures with larger grain sizes than the *poly*-In₂O₃ and In₂O₃:Me films, whereas the *spc*-In₂O₃:Me,H films with high Ce contents deposited at low $P_{\text{H}_2\text{O}}$ and all of the films deposited at high $P_{\text{H}_2\text{O}}$ exhibited polygonal and flower-like structures with substantially larger grains.

Figure 3 presents the θ -2 θ X-ray diffraction (XRD) patterns of the (a) glass substrate and *poly*-In₂O₃, In₂O₃:W, and In₂O₃:Ce films deposited at 200 °C and the as-deposited and *spc*-In₂O₃:H,

In₂O₃:W,H, and In₂O₃:Ce,H films deposited at $P_{\text{H}_2\text{O}}$ of (b) $\approx 2 \times 10^{-5}$ Pa and (c) $\approx 5 \times 10^{-5}$ Pa. The XRD patterns do not show evidence of segregation of the tungsten oxides and cerium oxides in the In₂O₃:Me and In₂O₃:Me,H films. All of the films deposited at 200 °C exhibited preferred orientation of the <111> direction (Figure 3(a)). However, an increase in $P_{\text{H}_2\text{O}}$ during deposition without substrate heating suppressed crystal growth. The as-deposited films deposited at low $P_{\text{H}_2\text{O}}$ ($\approx 2 \times 10^{-5}$ Pa) exhibited a very small 222 reflection with a broad peak originating from the amorphous structure (Figure 3(b)), whereas the films deposited at high $P_{\text{H}_2\text{O}}$ ($\approx 5 \times 10^{-5}$ Pa) exhibited amorphous structures without any diffraction peaks (Figure 3(c)). After the post-annealing process, a slight preferred orientation of the <111> direction was observed, especially for the *spc*-In₂O₃:H and In₂O₃:Me,H films with low Me contents deposited at low $P_{\text{H}_2\text{O}}$ (Figure 3(b)), indicating that small grains oriented in the <111> direction in the as-deposited films acted as crystalline nuclei during the crystallization process. By contrast, a more randomly oriented structure was observed for the *spc*-In₂O₃:Ce,H films with high CeO₂ contents (2 and 3 wt.%) deposited at low $P_{\text{H}_2\text{O}}$ (Figure 3(b)) and for the *spc*-In₂O₃:H and In₂O₃:Me,H films deposited at high $P_{\text{H}_2\text{O}}$ (Figure 3(c)). Figure 3(d) plots d values of the 444 reflection (d_{444}) for the films shown in Figure 3(a)–(c). The d_{444} values of the *poly*-In₂O₃ and In₂O₃:Me films were larger than that of the In₂O₃ powders ($d_{444} = 0.1460$ nm), indicating the formation of in-plane compressive strains in the films. By contrast, those of the *spc*-In₂O₃:H and In₂O₃:Me,H were nearly identical to that of the In₂O₃ powder, reflecting less-strained films. Furthermore, the crystallized films exhibited smaller full-width at half-maximum values of the 222 reflection than the films deposited at 200 °C, indicating larger crystallite sizes and smaller strains in the films. Notably, the large differences between the as-deposited polycrystalline films and solid-phase crystallized films do not originate from the slight difference in fabrication temperatures (i.e., 200 °C for the polycrystalline films and 250 °C for the solid-phase crystallized films) but from the different film-preparation methods.

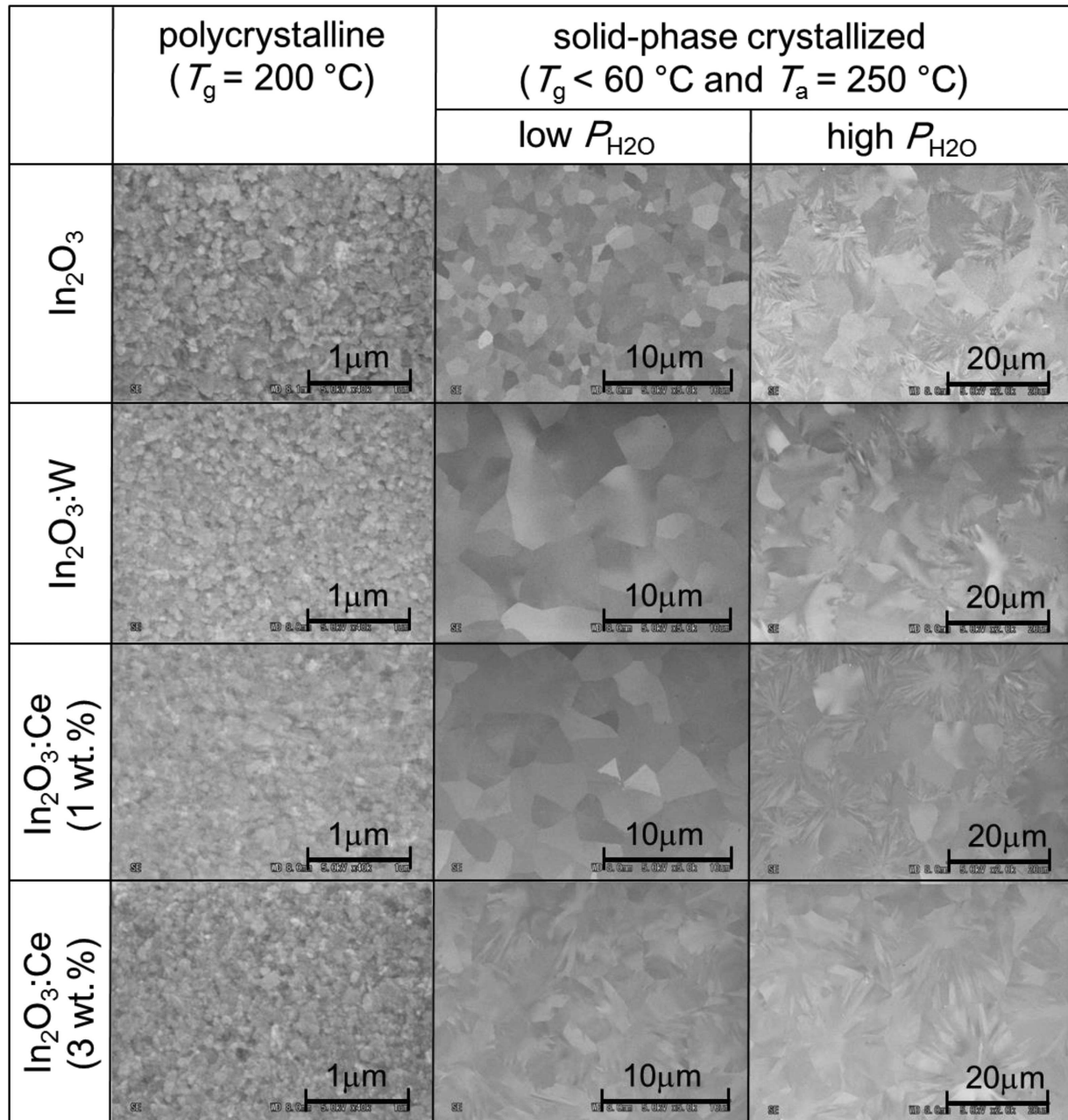


Figure 2. SEM images of the *poly*- In_2O_3 , $\text{In}_2\text{O}_3\cdot\text{W}$, $\text{In}_2\text{O}_3\cdot\text{Ce}$ (CeO_2 : 1 wt.%), and $\text{In}_2\text{O}_3\cdot\text{Ce}$ (CeO_2 : 3 wt.%) films deposited at $200\text{ }^\circ\text{C}$ and the *spc*- $\text{In}_2\text{O}_3\cdot\text{H}$, $\text{In}_2\text{O}_3\cdot\text{W}\cdot\text{H}$, $\text{In}_2\text{O}_3\cdot\text{Ce}\cdot\text{H}$ (CeO_2 : 1 wt.%), and $\text{In}_2\text{O}_3\cdot\text{Ce}\cdot\text{H}$ (CeO_2 : 3 wt.%) films deposited at low ($\approx 2 \times 10^{-5}\text{ Pa}$) and high ($\approx 5 \times 10^{-5}\text{ Pa}$) $P_{\text{H}_2\text{O}}$, respectively.

Electron backscatter diffraction (EBSD) mapping images revealed the orientation of each grain in the films. **Figure 4** presents (a) image quality maps and inverse pole figure maps along the (b) normal, (c) transverse, and (d) reference directions for the *spc*- $\text{In}_2\text{O}_3\cdot\text{H}$ films deposited at (1) low and (2) high $P_{\text{H}_2\text{O}}$. Here, the image quality map shows the GB and strain contrast. As observed in Figure 4(b-1, c-1, d-1), most of the grains in the film fabricated at low $P_{\text{H}_2\text{O}}$ were oriented in the $\langle 111 \rangle$ direction normal to the surface with the $\langle 101 \rangle$ direction parallel to the surface. This result corresponds well to the θ - 2θ pattern shown

in Figure 3(b). In addition, a dark spot within each grain is observed in the image quality map (Figure 4(a-1)). The difference in contrast reflects the difference in crystalline quality, indicating that the dark spots correspond to the crystalline nuclei embedded in the amorphous matrix, which were formed during deposition (Figure 3(b)). Hence, the map clearly suggests that the grain size ($\approx 0.81\text{ }\mu\text{m}$) of the post-annealed film was determined by the density of the crystalline nuclei and that no new nuclei were formed during post-annealing. Conversely, the film grown at high $P_{\text{H}_2\text{O}}$ exhibited larger grain sizes

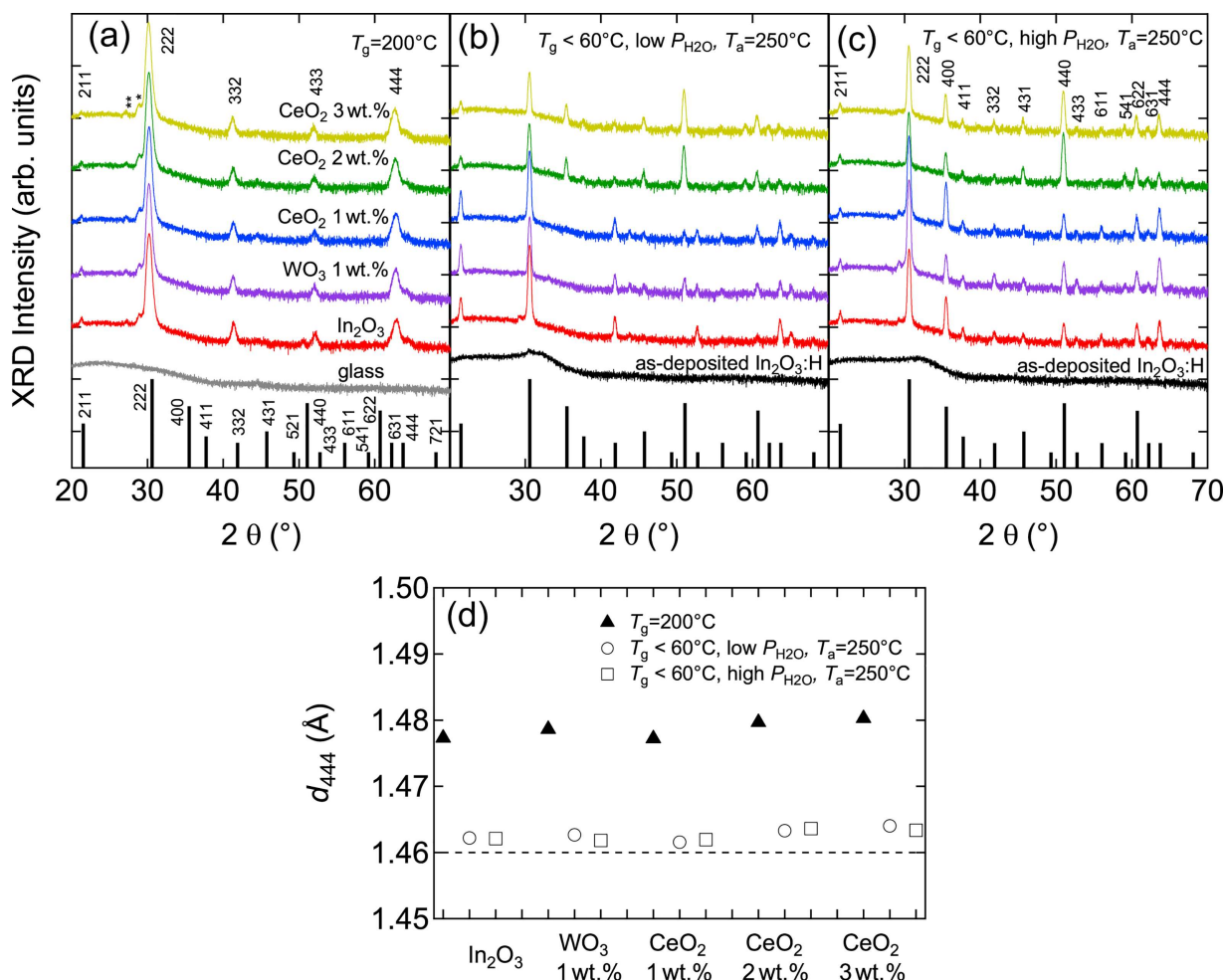


Figure 3. XRD θ - 2θ scan profiles for the (a) glass substrate, *poly*- In_2O_3 , $\text{In}_2\text{O}_3\text{:W}$, and $\text{In}_2\text{O}_3\text{:Ce}$ films deposited at 200°C , (b) as-deposited and *spc*- $\text{In}_2\text{O}_3\text{:H}$, $\text{In}_2\text{O}_3\text{:W,H}$, and $\text{In}_2\text{O}_3\text{:Ce,H}$ films deposited at $P_{\text{H}_2\text{O}} \approx 2 \times 10^{-5}$ Pa, and (c) as-deposited and *spc*- $\text{In}_2\text{O}_3\text{:H}$, $\text{In}_2\text{O}_3\text{:W,H}$, and $\text{In}_2\text{O}_3\text{:Ce,H}$ films deposited at $P_{\text{H}_2\text{O}} \approx 5 \times 10^{-5}$ Pa. The annealing temperature was 250°C . Stick patterns of In_2O_3 (JCPDS no. 6-416) are also shown for comparison. In (a), the two peaks denoted by “*” and “**” are 222 diffractions caused by Cu-K β and W-L lines caused by contamination of W from filaments, respectively. (d) Lattice spacing values of the (444) plane (d_{444}) for the films shown in (a)–(c).

($\approx 5.5 \mu\text{m}$) with random orientation normal and parallel to the surface. In contrast to Figure 4(a-1), Figure 4(a-2) shows no dark spots within the grains. In addition, the film crystallized at higher temperatures than the film grown at low $P_{\text{H}_2\text{O}}$, as will be explained in Section 2.2. Therefore, the formation of nuclei embedded in the amorphous matrix would be well suppressed because of the high $P_{\text{H}_2\text{O}}$ during deposition and crystalline nuclei would be formed during post-annealing.

On the basis of these results, we discuss the crystal growth of these films. All of the films deposited at 200°C exhibited preferred orientation in the $\langle 111 \rangle$ direction. Similar crystalline orientations have been observed in the XRD patterns of *poly*- In_2O_3 films deposited at 200°C and without substrate heating at a very low $P_{\text{H}_2\text{O}}$ of $< 5 \times 10^{-6}$ Pa for films prepared by magnetron sputtering.^[41,45] Because the (111) surface energy is the lowest among the low-indexed surfaces in In_2O_3 , including the (100), (110), and (111) surfaces,^[58] the films grown on glass would exhibit preferred orientation in the $\langle 111 \rangle$ direction. However, the introduction of larger amounts of Ce (CeO_2 : 2, 3 wt.%) and/

or H_2O vapor prevented the preferred orientation (Figure 3(b) and (c)). According to crystal growth theory, a critical cluster size exists because of the energy barrier that must be overcome for the cluster to grow to become a nucleus. Therefore, the incorporation of Ce and H atoms or OH-related species at the growth front influences medium-range structures^[59] in the amorphous films with an increase in the barrier height, thereby leading to the formation of low-density nuclei with preferred orientation of the $\langle 111 \rangle$ direction and no nuclei within the amorphous matrix at low and high $P_{\text{H}_2\text{O}}$, respectively. Consequently, the post-annealed films deposited at low and high $P_{\text{H}_2\text{O}}$ exhibited a slight preferred orientation of the $\langle 111 \rangle$ direction and random orientation, respectively. Here, in the latter films, nucleation would be generated from nanoclusters with medium-range ordering and grow during post-annealing. The grain size of the films deposited at high (low) $P_{\text{H}_2\text{O}}$ was $\approx 5.5 \mu\text{m}$ ($\approx 0.81 \mu\text{m}$), which are far larger than that ($\approx 0.44 \mu\text{m}$) of the films deposited via magnetron sputtering.^[47] This finding can be explained by the lower densities of crystalline nuclei in the

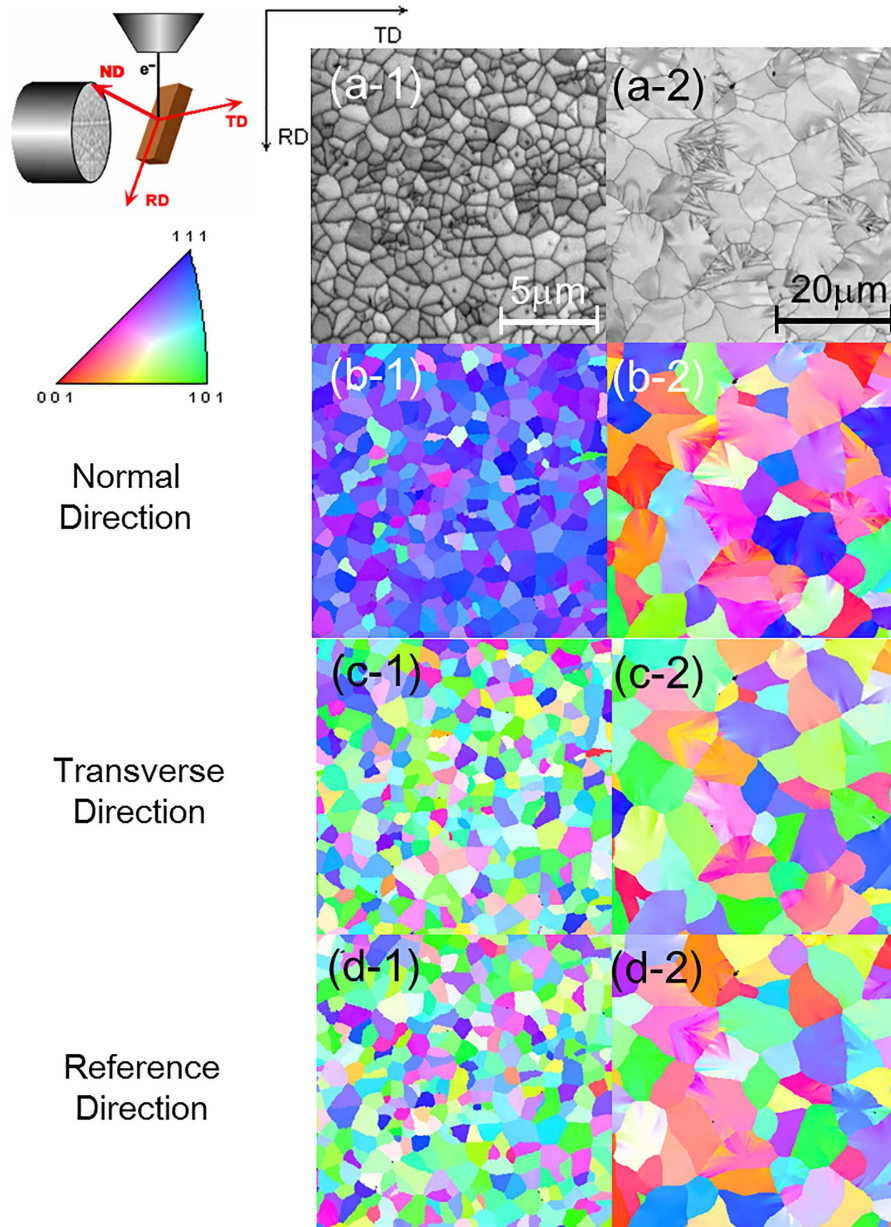


Figure 4. (a) Image quality maps and inverse pole figure maps along the (b) normal, (c) transverse, and (d) reference directions obtained using EBSD for the *spc*-In₂O₃:H films deposited at (1) low ($\approx 2 \times 10^{-5}$ Pa) and (2) high ($\approx 5 \times 10^{-5}$ Pa) $P_{\text{H}_2\text{O}}$.

as-deposited films deposited via RPD because the energy (<40 eV) of depositing particles (In, O, and O₂) during RPD^[60] is lower than that during magnetron sputtering.

2.2. Electrical Properties

Figure 5 shows the change in N and μ during heating and subsequent cooling for the as-deposited (a) In₂O₃:H films, (b) In₂O₃:W,H films, (c) In₂O₃:Ce,H (CeO₂: 1 wt.%) films, (d) In₂O₃:Ce,H (CeO₂: 2 wt.%) films, and (e) In₂O₃:Ce,H (CeO₂: 3 wt.%) films deposited at high and low $P_{\text{H}_2\text{O}}$. The electrical properties of the films were measured during heating from 40 to 250 °C and

subsequent cooling from 250 °C to room temperature under vacuum. During heating, solid-phase crystallization occurred. In **Figure 5(a)**, the as-deposited *a*-In₂O₃:H films grown at high $P_{\text{H}_2\text{O}}$ exhibited a constant N at temperatures below 180 °C, indicating that the film was a degenerately doped semiconductor. However, a large decrease in N combined with an increase in μ was clearly observed at 180–200 °C. Previous XRD and SEM analyses for *a*-In₂O₃:H films deposited via magnetron sputtering revealed that crystallization proceeded at the temperatures at which the N and μ values varied.^[47] Therefore, the change observed in **Figure 5(a)** originated from the increase in the volume fraction of the crystalline phase in the film. Upon full crystallization, the film exhibited a constant N at temperatures over the entire range and

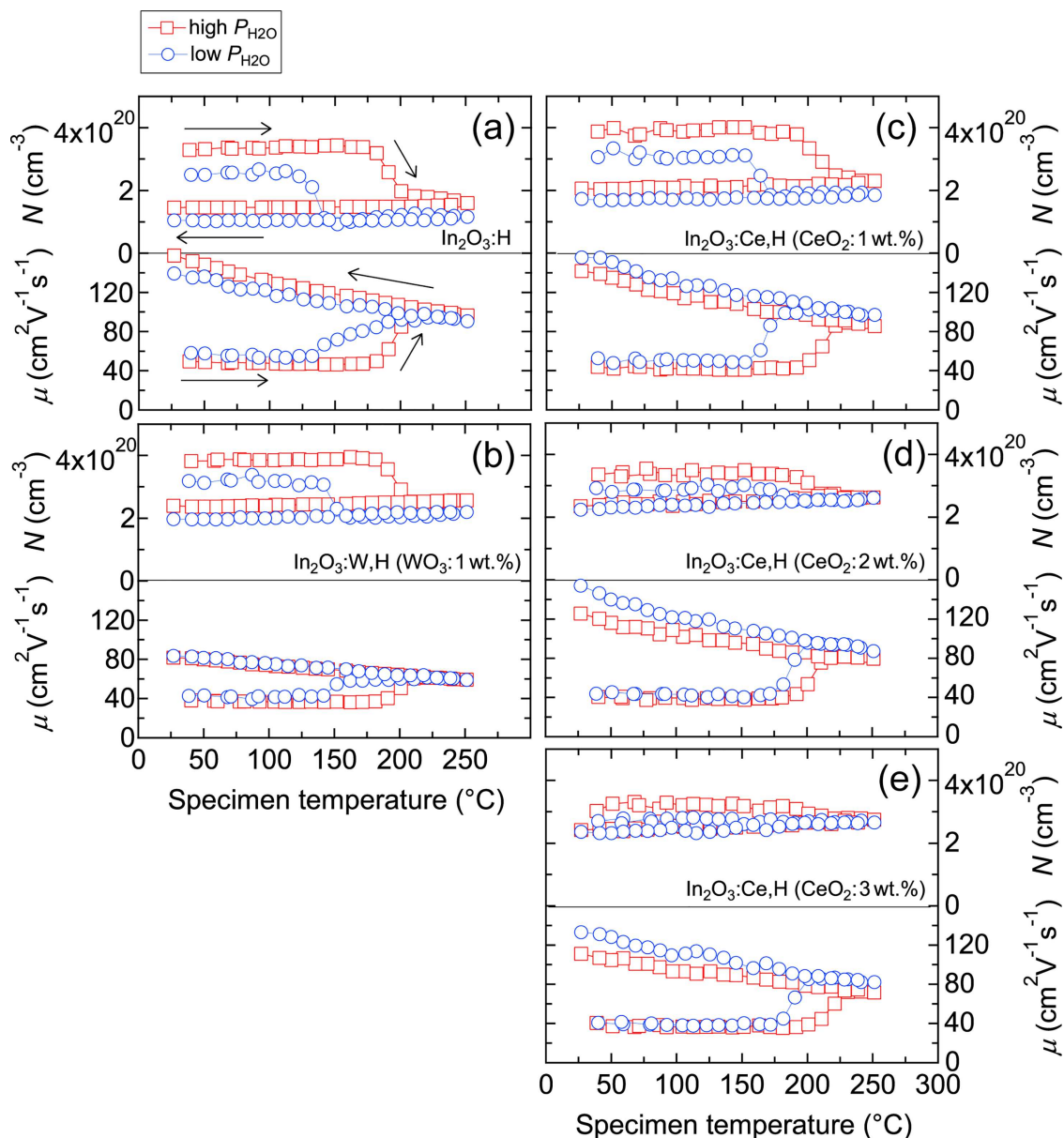


Figure 5. Carrier density (N) and mobility (μ) as a function of specimen temperature for the (a) $\text{In}_2\text{O}_3:\text{H}$, (b) $\text{In}_2\text{O}_3:\text{W,H}$ (WO_3 : 1 wt.%), (c) $\text{In}_2\text{O}_3:\text{Ce,H}$ (CeO_2 : 1 wt.%), (d) $\text{In}_2\text{O}_3:\text{Ce,H}$ (CeO_2 : 2 wt.%), and (e) $\text{In}_2\text{O}_3:\text{Ce,H}$ (CeO_2 : 3 wt.%) films deposited at high ($\approx 5 \times 10^{-3}$ Pa) and low ($\approx 2 \times 10^{-5}$ Pa) $P_{\text{H}_2\text{O}}$. The electrical properties were measured during heating from 40 to 250 °C and subsequent cooling from 250 °C to room temperature. During heating to 250 °C, solid-phase crystallization occurred.

an increase in μ with decreasing temperature. In the as-deposited $a\text{-In}_2\text{O}_3:\text{H}$ films grown at low $P_{\text{H}_2\text{O}}$, the change in N occurred at lower temperatures (130–150 °C), which can be explained by the presence of abundant crystalline nuclei within the as-deposited film described in Section 2.1, thereby leading to full crystallization at lower temperatures. This finding is also true for the $a\text{-In}_2\text{O}_3:\text{W,H}$ and $a\text{-In}_2\text{O}_3:\text{Ce,H}$ films with a small amount of Ce (Figure 5(b) and (c)). However, the temperature increased with increasing Ce content (Figure 5(c)–(e)): i.e., 160–180 °C (200–220 °C) for $\text{In}_2\text{O}_3:\text{Ce,H}$ (CeO_2 : 1 wt.%) films, 180–200 °C (190–210 °C) for $\text{In}_2\text{O}_3:\text{Ce,H}$ (CeO_2 : 2 wt.%) films, and 180–200 °C (210–230 °C) for $\text{In}_2\text{O}_3:\text{Ce,H}$ (CeO_2 : 3 wt.%) films

deposited at low (high) $P_{\text{H}_2\text{O}}$. The Ce doping increased the crystallization temperature.

As shown in Figure 5, all of the as-deposited films exhibited higher N values when deposited at high $P_{\text{H}_2\text{O}}$. In general, the N of $a\text{-In}_2\text{O}_3$ -based TCOs, including $a\text{-IZO}$, $a\text{-ITO}$, and $a\text{-In}_2\text{O}_3:\text{H}$, can be controlled by the oxygen deficiency in the film.^[59,61] Herein, only $P_{\text{H}_2\text{O}}$ was varied; the O_2 and Ar flow rates were constant. Therefore, the oxygen deficiency in the film increased with increasing $P_{\text{H}_2\text{O}}$ because of the presence of H radicals and ions produced in the plasma during deposition. Here, we assume that the N values in the $a\text{-In}_2\text{O}_3:\text{H}$ and $a\text{-In}_2\text{O}_3:\text{Me,H}$ films were basically determined by the oxygen stoichiometry

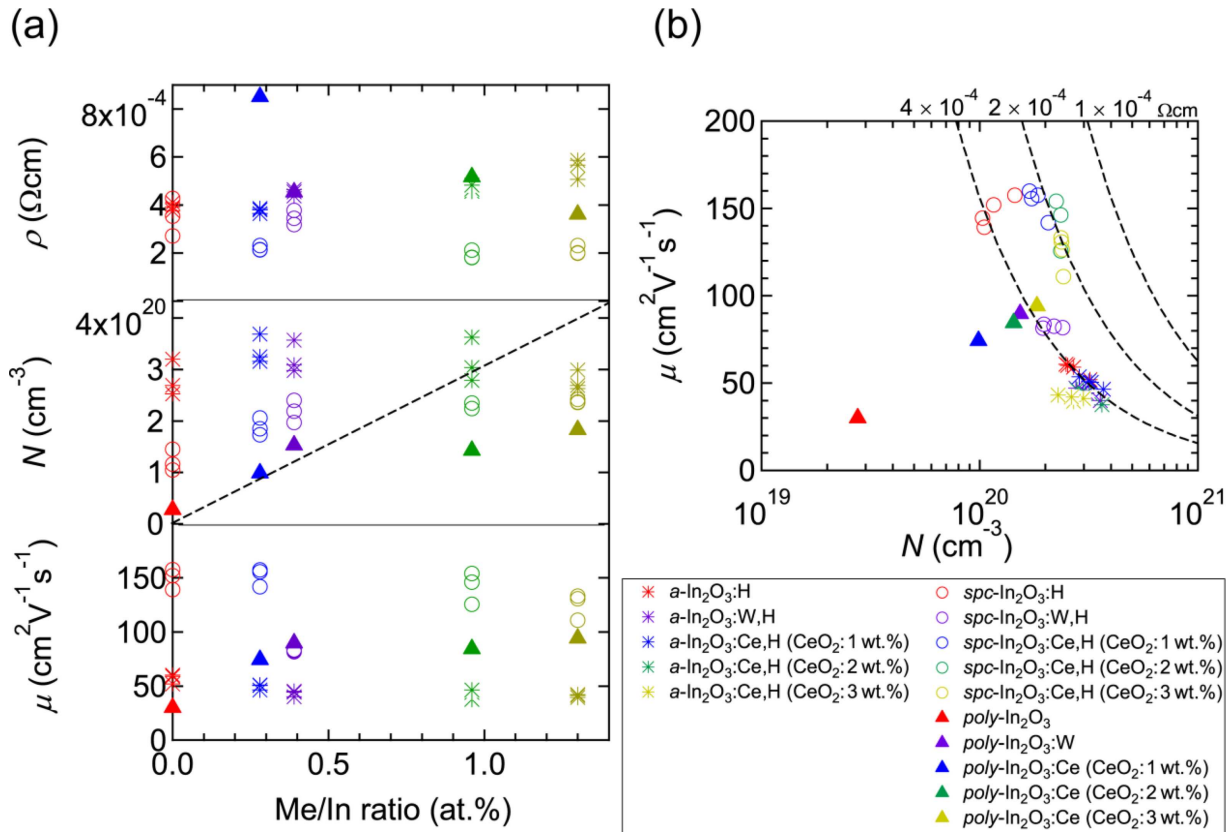


Figure 6. (a) Resistivity (ρ), carrier density (N), and mobility (μ) as a function of Me/In ratio for the $\text{poly-In}_2\text{O}_3$, $\text{In}_2\text{O}_3\text{:W}$, and $\text{In}_2\text{O}_3\text{:Ce}$ films deposited at 200°C , the $a\text{-In}_2\text{O}_3\text{:H}$, $\text{In}_2\text{O}_3\text{:W,H}$, and $\text{In}_2\text{O}_3\text{:Ce,H}$ films deposited without substrate heating, and the $\text{spc-In}_2\text{O}_3\text{:H}$, $\text{In}_2\text{O}_3\text{:W,H}$, and $\text{In}_2\text{O}_3\text{:Ce,H}$ films post-annealed at 250°C . (b) Relationship between carrier density and mobility for the films. The amorphous films were deposited at $P_{\text{H}_2\text{O}}$ broadly ranging from $\approx 1 \times 10^{-5}$ to $\approx 7 \times 10^{-5}$ Pa, as shown in Figure 1.

rather than by the H contents because we confirmed that the incorporation of H in sputtered $a\text{-IZO}$ did not influence the transport properties^[62]: $a\text{-IZO}$ films deposited without intentional introduction of H_2O vapor ($< 5 \times 10^{-6}$ Pa) exhibited almost the same N and μ values as the $a\text{-IZO:H}$ (H: ≈ 3 at.%) films deposited at $P_{\text{H}_2\text{O}}$ of $\approx 1.5 \times 10^{-4}$ Pa, and the N values in both films decreased with increasing O_2 -to-Ar flow ratio during sputtering.

Figure 6(a) summarizes the ρ , N , and μ values as a function on the Me/In ratio for the as-deposited amorphous films, solid-phase crystallized films at 250°C , and polycrystalline films deposited at 200°C . The dotted line in the middle panel of Figure 6(a) shows the expected N for which all the carriers are generated by singly charged donors (e.g., $\text{Me}_{\text{In}}^\bullet$, $\text{W}_{\text{In}}^{\bullet\bullet\bullet}\text{O}_i^{\bullet\bullet}$). As observed in the middle panel of Figure 6(a), N of the amorphous films did not increase with increasing Me/In ratio and instead decreased with increasing Ce/In ratio. The results clearly demonstrate that Me did not act as an electron donor in the amorphous phase and that Ce doping reduced the oxygen deficiency within the $a\text{-In}_2\text{O}_3$ matrix, likely because of the higher bond strength of Ce–O than In–O. Moreover, the μ values decreased with increasing Ce content, indicating that Ce atoms act as scattering centers for free electrons in the amorphous structure.

As shown in Figure 5(a), upon crystallization of the $\text{In}_2\text{O}_3\text{:H}$ layer, N decreased with a large increase in μ . In addition, the slope of mobility as a function of temperature increased after crystallization. These results suggest a change in the carrier generation and scattering mechanisms. In previous works, we proposed that structural rearrangements during crystallization eliminate oxygen-vacancy-type defects with a large scattering cross section and produce H_i^\bullet and/or $\text{H}_\text{O}^\bullet$, which act as singly charged donors.^[41,47] In $\text{In}_2\text{O}_3\text{:W,H}$ and $\text{In}_2\text{O}_3\text{:Ce,H}$ films, decreases of N were observed at the crystallization temperatures. However, the magnitude of the decreases of N decreased with increasing Me contents. As shown in the middle panel of Figure 6(a), the N values of the crystallized $\text{In}_2\text{O}_3\text{:H}$ films were $\approx 1 \times 10^{20}$ – $1.5 \times 10^{20} \text{ cm}^{-3}$ because of the H_i^\bullet and/or $\text{H}_\text{O}^\bullet$ donors. As the Me content was increased to 0.39 at.%, the N values increased with a similar slope of the dotted line. A further increase of the Ce content resulted in a gradual increase of the N values. These results demonstrate that W and Ce were activated as donors by the crystallization process even in the presence of hydrogen. By contrast, the N of the $\text{poly-In}_2\text{O}_3$ film deposited at 200°C was $3 \times 10^{19} \text{ cm}^{-3}$. The free carriers are assumed to be generated from intrinsic defects, mainly from oxygen-vacancy-type defects, as revealed in previous works.^[34,44] When the films were doped with low Me contents, the N values increased in

accordance with the dotted line. A further increase in the Ce/In ratio increased the N values although the values were below the dotted line. These results indicate that W and Ce work as electron donors.

The overall behavior of N as a function of the Me/In ratio for the *spc*-In₂O₃:H and In₂O₃:Me,H films was the same as that for the *poly*-In₂O₃ and In₂O₃:Me films with an N offset of $\approx 1 \times 10^{20} \text{ cm}^{-3}$. This result strongly suggests that the offset is produced by H_i^\bullet and/or $\text{H}_\text{O}^\bullet$ donors. Notably, the H contents determined by TDS and hydrogen forward-scattering spectrometry (HFS) reveal that large amounts of hydrogen are present that do not contribute to the carrier generation. The hydrogen passivates acceptors^[56] to reduce the carrier compensation because the In₂O₃:H and In₂O₃:Ce,H films exhibited significantly high μ , as described below.

We here focus on the μ values of the films. Figure 6(b) summarizes the relationship between N and μ measured at room temperature for the as-deposited amorphous films, solid-phase crystallized films at 250 °C, and polycrystalline films deposited at 200 °C. At a glance, the μ values varied depending on the film structure and fabrication processes: the *a*-In₂O₃:H and In₂O₃:Me,H films exhibited μ values of $40\text{--}60 \text{ cm}^2 \text{ V}^{-1} \text{ s}^{-1}$, the *poly*-In₂O₃ and In₂O₃:Me films exhibited μ values of $30\text{--}90 \text{ cm}^2 \text{ V}^{-1} \text{ s}^{-1}$ that strongly depended on Me, the *spc*-In₂O₃:H and In₂O₃:Ce,H films exhibited μ values of $110\text{--}160 \text{ cm}^2 \text{ V}^{-1} \text{ s}^{-1}$, and the *spc*-In₂O₃:W,H films exhibited μ values of $\approx 80 \text{ cm}^2 \text{ V}^{-1} \text{ s}^{-1}$. In general, the mobility of polycrystalline TCO films is dominated by scattering produced by GBs, stacking faults, dislocations, point defects including ionized and neutral impurities, and phonons.^[51,52] To distinguish between the contributions of the various scattering sources, a comparison of the Hall and optical mobilities and measurements of the temperature dependence of the Hall effect are useful. The ratio between the Hall mobility and the optical mobility reflects the effect of GB scattering: a ratio of 1 implies that GB scattering plays a negligible effect in the films, whereas a ratio less than 1 implies that GB scattering influences the μ values, as explained in Section 1. When transport across GBs occurs mainly through thermionic emission instead of tunneling, the effect of GB scattering on the μ values increases with decreasing temperature.^[51–53] This trend is also true for scattering induced by charged extended defects.^[52] By contrast, scattering induced by ionized and neutral impurities is independent of temperature in a degenerately doped semiconductor, whereas phonon scattering becomes large with increasing temperature. From a previous analysis of *spc*-In₂O₃:H films that exhibit transport properties similar to those shown in Figure 6, the Hall mobilities were equal to the optical mobilities,^[47] suggesting that GB scattering plays a negligible effect and that intragrain properties limit the Hall mobilities in the *spc*-In₂O₃:H films.

Figure 7 shows a plot of the data in Figure 5 for the *spc*-In₂O₃:H and In₂O₃:Me,H films during the cooling process from 250 °C to room temperature; the mobilities are plotted versus the corresponding carrier densities with temperature acting as parameter. The *spc*-In₂O₃:H and *spc*-In₂O₃:Ce,H (CeO₂: 1 wt.%) films exhibited i) a slight decrease in N with an increase in μ from 250 to 230 °C and ii) a large increase in μ with a negligible change in N from 230 °C to room temperature. The former result is explained by the desorption of H from the films during

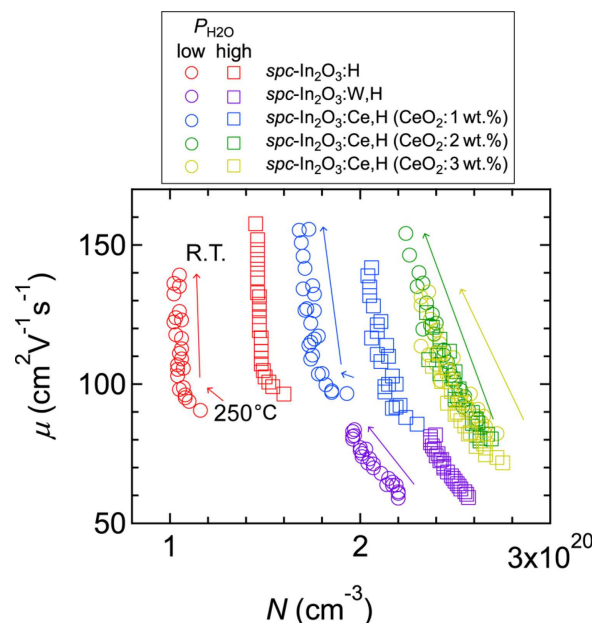


Figure 7. Variation of the carrier density (N) and mobility (μ) of *spc*-In₂O₃:H, In₂O₃:W,H, and In₂O₃:Ce,H films during cooling from 250 °C to room temperature. The data are replotted from that shown in Figure 5. The films were deposited at high ($\approx 5 \times 10^{-5}$ Pa, squares) and low ($\approx 2 \times 10^{-5}$ Pa, circles) $P_{\text{H}_2\text{O}}$ levels.

heating under vacuum, whereas the latter result clearly suggests that phonon scattering dominates the films' μ values. The *spc*-In₂O₃:H film deposited at high $P_{\text{H}_2\text{O}}$ and the *spc*-In₂O₃:Ce,H (CeO₂: 1 wt.%) film deposited at low $P_{\text{H}_2\text{O}}$ exhibited high μ values of $\approx 160 \text{ cm}^2 \text{ V}^{-1} \text{ s}^{-1}$ at room temperature. The high μ values with N values of $\approx 1 \times 10^{20}\text{--}2 \times 10^{20} \text{ cm}^{-3}$ cannot be quantitatively explained by the current models,^[49] as described in Section 1. However, the μ values strongly suggest that scattering produced by neutral and doubly charged ionized impurities is negligible and that their mobilities are limited by singly charged donors (e.g., $\text{Ce}_{\text{In}}^\bullet$, H_i^\bullet , $\text{H}_\text{O}^\bullet$) and by phonon scattering.^[49] Indeed, the dominant valence states of Ce have been reported to be 3+ and 4+ in In₂O₃:Ce,H and In₂O₃:Ce films.^[6] Conversely, the μ values for the *spc*-In₂O₃:H film deposited at low $P_{\text{H}_2\text{O}}$ increased slowly with decreasing temperature and the film exhibited lower μ values at room temperature than the film deposited at high $P_{\text{H}_2\text{O}}$. Plausibly, charged extended and point defects within grains are present in the film because of low H contents and/or H effusion from the film during post-annealing. Indeed, decreases in both the Hall and the optical mobility were observed in *spc*-In₂O₃:H films when the films were post-annealed at higher temperatures (400 °C).^[47] By contrast, the μ values of the *spc*-In₂O₃:Ce,H films with high Ce contents increased and N decreased during cooling from 250 °C to room temperature. A further increase of the Ce content resulted in a large decrease of μ and a slight increase of N (Figure 6 and 7). These results imply that extensive Ce doping (Ce/In $\geq 0.96\%$) produced carrier scattering centers in addition to the singly charged donors (e.g., $\text{Ce}_{\text{In}}^\bullet$, H_i^\bullet , $\text{H}_\text{O}^\bullet$), leading to compensation of the free carriers, likely via the formation of defect complexes such as $2 \text{ Ce}_{\text{In}}^\bullet \text{ O}_i''$ in the films. By contrast, *spc*-In₂O₃:W,H

exhibited much lower μ values at 250 °C and room temperature, indicating that W doping produces other scattering centers. Because no large difference in the structure was detected between the *spc*-In₂O₃:W,H and *spc*-In₂O₃:H films by XRD, SEM, and transmission electron microscopy (TEM) (not shown here) analyses, the point defects within the grains that cannot be assessed by these characterization tools may be responsible for the low mobility. In addition, post-annealing of the *poly*-In₂O₃:W film at 300 °C increased the μ values to 110 cm² V⁻¹ s⁻¹, much higher than the μ values of the *spc*-In₂O₃:W,H films, as will be shown later. The same post-annealing process was performed for the *spc*-In₂O₃:W,H films; however, the μ values of the films did not increase (not shown here). Therefore, point defects associated with W and H or OH species may be responsible for the other scattering centers produced in the *spc*-In₂O₃:W,H films.

With respect to the carrier scattering in the *poly*-In₂O₃:Me films, Figure 6(a) and (b) shows that the μ values of the *poly*-In₂O₃:Ce films were much smaller than those of the corresponding *spc*-In₂O₃:Ce,H films. To investigate the dominant scattering centers in the polycrystalline films, we post-annealed the films at 300 °C. The [N (cm⁻³), μ (cm² V⁻¹ s⁻¹)] values varied from [1.7×10^{20} , 82] to [1.7×10^{20} , 110], from [1.1×10^{20} , 70] to [1.1×10^{20} , 96], from [1.5×10^{20} , 81] to [1.5×10^{20} , 100], and from [1.9×10^{20} , 88] to [2.0×10^{20} , 110] after the post-annealing process for the *poly*-In₂O₃:W, *poly*-In₂O₃:Ce (CeO₂: 1 wt.%), *poly*-In₂O₃:Ce (CeO₂: 2 wt.%), and *poly*-In₂O₃:Ce (CeO₂: 3 wt.%) films, respectively. In all of the films, μ values increased with a negligible change in N . The mobility improvement was not accompanied by a change of the structural properties, as revealed by XRD (not shown). Thus, no recrystallization occurred during the post-annealing process. However, the point and extended defect densities were plausibly reduced by the process. That is, the as-deposited *poly*-In₂O₃:Me films contained a large amount of point and extended defects because of the low-temperature deposition and their mobilities were limited largely by intragrain properties. Notably, a linear increase of μ values with increasing N in Figure 6(b) for the as-deposited *poly*-In₂O₃ and In₂O₃:Me films seems like a suggestion at a glance that the GB scattering strongly influences the μ values if we assume similar grain sizes and trap densities at GBs in the polycrystalline films. However, the aforementioned changes in transport properties induced by post-annealing clearly suggest that the μ values in the *poly*-In₂O₃:Me films were limited by intragrain properties rather than by grain barriers.

Finally, we discuss the role of solid-phase crystallization and H doping in the In₂O₃:H and In₂O₃:Me,H films. The *spc*-In₂O₃:H and In₂O₃:Ce,H films exhibited μ values greater than those of the *poly*-In₂O₃ and In₂O₃:Ce films. In addition, the *spc*-In₂O₃:H and In₂O₃:Ce,H (CeO₂: 1 wt.%) films exhibited increases in μ with negligible changes in N during cooling from 250 °C to room temperature. These results suggest that solid-phase crystallization substantially reduced scattering by GBs and extended and point defects within grains. These findings are attributed to fewer lattice defects because of the use of solid-phase crystallization instead of low-temperature crystal growth by physical vapor deposition. This finding is supported by the structural properties explained in Section 2.1. By contrast, H doping increased N . As observed in the middle panel of Figure 6

(a), the overall behavior of N as a function of the Me/In ratio for the *spc*-In₂O₃:H and In₂O₃:Me,H films was the same as that for the *poly*-In₂O₃ and In₂O₃:Me films with an N offset of $\approx 1 \times 10^{20}$ cm⁻³. This result strongly suggests that the offset is produced by H_i[•] and/or H_o[•] donors and by reduced carrier compensation through passivation of acceptors by hydrogen. Notably, the presence of hydrogen within the films did not prevent activation of the Ce donors. However, further Ce doping (Ce/In $\geq 0.96\%$) resulted in saturation of N in conjunction with a decrease of μ . Conversely, W doping in In₂O₃:H apparently produced additional carrier scattering centers, as previously described. These results suggest that room may exist for further increasing N while maintaining a high μ by selecting appropriate metal dopants.

2.3. Optical Properties

Figure 8 presents the optical constants for the (a) *a*-In₂O₃:H and In₂O₃:Me,H films, (b) *poly*-In₂O₃ and In₂O₃:Me films, and (c) *spc*-In₂O₃:H and In₂O₃:Me,H films, as evaluated by spectroscopic ellipsometry. As observed in the extinction coefficient (k) spectra, all of the films were transparent in the visible and near-infrared (NIR) regions. In the longer-wavelength region (>1200 nm), k increased with increasing N because of free-carrier absorption. In addition, the refractive index (n) of the films shifted toward lower values in the NIR region with increasing N , consistent with the Drude model. In the ultraviolet region, all of the films exhibited strong absorption. Figure 9 shows the absorption coefficients ($\alpha = 4\pi k/\lambda$) for the (a) *a*-In₂O₃:H and In₂O₃:Me,H films, (b) *poly*-In₂O₃ and In₂O₃:Me films, and (c) *spc*-In₂O₃:H and In₂O₃:Me,H films. All of the films exhibited absorption onsets at 2.7–2.8 eV. The α values steeply increased to greater than 10⁵ cm⁻¹ at photon energies of 3.8–4.0 eV, and the absorption varied depending on the dopant species in the amorphous, polycrystalline, and solid-phase crystallized films. The absorption edges increased with increasing N (Figure 6(a)) in the amorphous, polycrystalline, and solid-phase crystallized films; this behavior is well explained by the Burstein–Moss shift.

Next, we will consider the weaker absorption extending from the photon energies of 3.8–4.0 eV to the onset energies of 2.7–2.8 eV. In In₂O₃, a strong optical absorption at ca. 3.7 eV in the ultraviolet was assigned to a direct transition, whereas an onset of weaker optical absorption at ca. 2.6 eV was assigned to an indirect transition from the valence-band maximum (VBM) away from the Γ -point to the conduction-band minimum (CBM) at the Γ -point.^[63] However, recent first-principles calculations and photoemission spectroscopy have revealed that there is no nature of indirect transition.^[64–66] Specifically, optical transitions at ca. 2.9 eV from the VBM to the CBM at the Γ -point are forbidden by the symmetry of the bixbyite crystal, whereas optical transitions at ca. 3.7 eV from the lower-lying valence-band states (≈ 0.8 eV below the VBM) to the CBM are parity-allowed.^[64] Figure 9(d) shows a plots of the α values of the films as a function of the photon energy on a logarithmic scale. The *spc*-In₂O₃:H film showed an α value much less than 10³ cm⁻¹ at ≈ 3 eV and exhibited an absorption onset of 2.7–2.8 eV. This result is in good agreement with the α spectra of bulk In₂O₃ crystals,^[63,67] suggesting high crystalline quality in the *spc*-

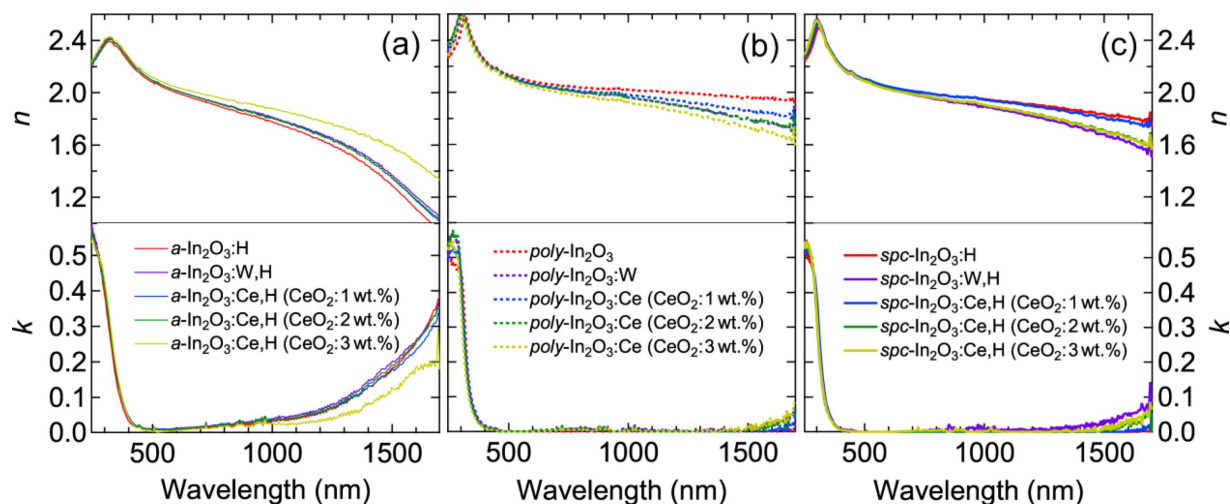


Figure 8. Refractive index (n) and extinction coefficient (k) as a function of wavelength for the (a) a - In_2O_3 :H, In_2O_3 :W,H, and In_2O_3 :Ce,H films, (b) $\text{poly-In}_2\text{O}_3$, In_2O_3 :W, and In_2O_3 :Ce films, and (c) $\text{spc-In}_2\text{O}_3$:H, In_2O_3 :W,H, and In_2O_3 :Ce,H films. The crystallized films were deposited at high ($\approx 5 \times 10^{-5}$ Pa) $P_{\text{H}_2\text{O}}$.

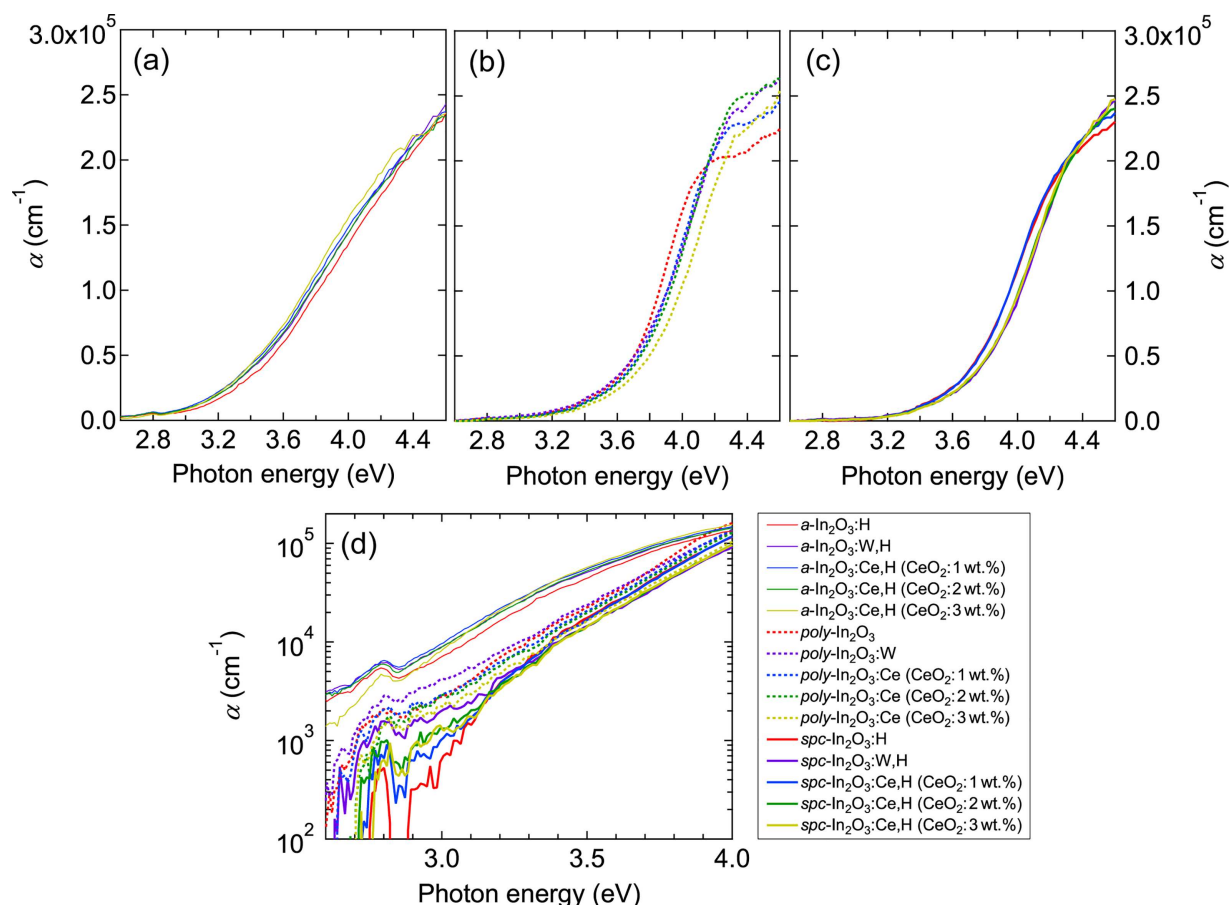


Figure 9. Absorption coefficients (α) as a function of photon energy for the (a) a - In_2O_3 :H, In_2O_3 :W,H, and In_2O_3 :Ce,H films, (b) $\text{poly-In}_2\text{O}_3$, In_2O_3 :W, and In_2O_3 :Ce films, and (c) $\text{spc-In}_2\text{O}_3$:H, In_2O_3 :W,H, and In_2O_3 :Ce,H films. (d) α values as a function of photon energy for the films on a logarithmic scale. The crystallized films were deposited at high ($\approx 5 \times 10^{-5}$ Pa) $P_{\text{H}_2\text{O}}$.

$\text{In}_2\text{O}_3:\text{H}$ film. In addition, the onset energy reflects an indirect fundamental bandgap. The direct forbidden transitions weakly allowed away from the Γ -point may contribute to the absorption.^[64–66] When compared with the spectra of the *spc*- $\text{In}_2\text{O}_3:\text{H}$ and *poly*- In_2O_3 films, that of the *poly*- In_2O_3 film exhibited milder slopes; in addition, the *poly*- In_2O_3 film exhibited a higher α value than the *spc*- $\text{In}_2\text{O}_3:\text{H}$ film at ≈ 3 eV. Here, the slight shift of the α spectra along the horizontal axis is attributed to the difference in N values, as previously explained. The milder slope with higher α values reflects the existence of defect states in the *poly*- In_2O_3 film. In addition, the structural disorder might weaken the selection rule of the direct forbidden transitions, giving rise to weak but non-negligible transitions. Furthermore, optical transitions that are forbidden by the selection rules could occur in the disordered structure of the *a*- $\text{In}_2\text{O}_3:\text{H}$ film, leading to α values much higher than those of the *spc*- $\text{In}_2\text{O}_3:\text{H}$ and *poly*- In_2O_3 films. Notably, the *spc*- $\text{In}_2\text{O}_3:\text{W,H}$ and *poly*- $\text{In}_2\text{O}_3:\text{W}$ films exhibited higher α values at ≈ 3 eV than other crystallized and polycrystalline films, respectively, even though the W-doped films exhibited crystallinity comparable to the other films, as revealed by the SEM, XRD, and TEM analyses. The greater absorption in the W-doped films may originate from W d-states.^[68]

3. Conclusion

Two types of In_2O_3 films with mobilities substantially greater than that of ITO were recently reported. *Poly*- In_2O_3 films doped with metal (Ti, Zr, Mo, or W) impurities instead of Sn exhibited mobilities greater than $\approx 80 \text{ cm}^2 \text{ V}^{-1} \text{ s}^{-1}$ even when grown at low temperatures, and *spc*- $\text{In}_2\text{O}_3:\text{H}$ and $\text{In}_2\text{O}_3:\text{Ce,H}$ films fabricated at low temperatures exhibited mobilities greater $\approx 100 \text{ cm}^2 \text{ V}^{-1} \text{ s}^{-1}$. To determine the effect of the i) metal dopant species; ii) metal and H codoping; and iii) solid-phase crystallization process on the resultant transport properties, we fabricated *poly*- In_2O_3 , $\text{In}_2\text{O}_3:\text{W}$, and $\text{In}_2\text{O}_3:\text{Ce}$ films on glass substrates at 200°C and *spc*- $\text{In}_2\text{O}_3:\text{H}$, $\text{In}_2\text{O}_3:\text{W,H}$, and $\text{In}_2\text{O}_3:\text{Ce,H}$ films post-annealed at 250°C via RPD. The obtained $[N (\text{cm}^{-3}), \mu (\text{cm}^2 \text{ V}^{-1} \text{ s}^{-1})]$ values were $[2.8 \times 10^{19}, 30]$, $[1.5 \times 10^{20}, 90]$, $[9.9 \times 10^{19}, 74]$, $[1.4 \times 10^{20}, 85]$, and $[1.8 \times 10^{20}, 94]$ for the *poly*- In_2O_3 , $\text{In}_2\text{O}_3:\text{W}$ (WO_3 : 1 wt.%), and $\text{In}_2\text{O}_3:\text{Ce}$ (CeO_2 : 1, 2, and 3 wt.%) films, respectively, whereas these values were $[1.1 \times 10^{20} - 1.5 \times 10^{20}, 140 - 160]$, $[2.0 \times 10^{20} - 2.4 \times 10^{20}, 82 - 84]$, $[1.7 \times 10^{20} - 2.1 \times 10^{20}, 140 - 160]$, $[2.2 \times 10^{20} - 2.4 \times 10^{20}, 130 - 150]$, and $[2.4 \times 10^{20}, 110 - 130]$ for the *spc*- $\text{In}_2\text{O}_3:\text{H}$, $\text{In}_2\text{O}_3:\text{W,H}$ (WO_3 : 1 wt.%) and $\text{In}_2\text{O}_3:\text{Ce,H}$ (CeO_2 : 1, 2, and 3 wt.%) films, respectively. The N values of the crystallized films were $\approx 1 \times 10^{20} \text{ cm}^{-3}$ higher than those of the corresponding films, indicating that H doping produces $\approx 1 \times 10^{20} \text{ cm}^{-3}$ free electrons. In addition, Ce and W doping increased the carrier density with increasing Me/In ratio in both *spc*- $\text{In}_2\text{O}_3:\text{Me,H}$ and *poly*- $\text{In}_2\text{O}_3:\text{Me}$ deposited at 200°C , suggesting that Ce and W function as electron donors and that the presence of H in the films does not affect their carrier activation. Analysis of the N - μ and μ -temperature behaviors of the *spc*- $\text{In}_2\text{O}_3:\text{Me,H}$ and $\text{In}_2\text{O}_3:\text{Ce,H}$ films strongly supported the hypothesis that the free carriers were generated by singly charged donors (e.g., H_i^\bullet , H_o^\bullet , $\text{Ce}_{\text{In}}^\bullet$) and that scattering induced by the ionized

impurities and phonons dominated their μ values. Conversely, the *spc*- $\text{In}_2\text{O}_3:\text{W,H}$ films exhibited a lower mobility of $\approx 80 \text{ cm}^2 \text{ V}^{-1} \text{ s}^{-1}$. The structural and electrical analyses and comparative studies between the *spc*- $\text{In}_2\text{O}_3:\text{W,H}$ and *poly*- $\text{In}_2\text{O}_3:\text{W}$ films suggested the presence of point defects associated with W and H or OH species in the *spc*- $\text{In}_2\text{O}_3:\text{W,H}$ films. By contrast, *poly*- In_2O_3 and $\text{In}_2\text{O}_3:\text{Ce}$ exhibited lower μ values than the *spc*- $\text{In}_2\text{O}_3:\text{H}$ and $\text{In}_2\text{O}_3:\text{Ce,H}$ films, respectively. Changes in the N and μ values after the post-annealing process indicated that the mobility of the as-deposited polycrystalline films was strongly limited by intragrain properties, i.e., scattering centers produced by stacking faults, dislocations, and point defects. Indeed, the SEM, TEM, and XRD analyses revealed that the films had small grains with abundant lattice defects, in sharp contrast to the case of crystallized films with large grains with high crystallinity. Furthermore, the films exhibited larger absorption tails at ≈ 3 eV compared with those of the crystallized films. These results strongly suggest that the solid-phase crystallization process serves to substantially improve the intragrain properties. Furthermore, EBSD analysis revealed that the $P_{\text{H}_2\text{O}}$ and the Me contents during deposition determined the density of the crystalline nuclei within the as-deposited amorphous films and, thus, also determined the grain size of the crystallized films.

4. Experimental Section

Approximately 60-nm-thick and 220-nm-thick In_2O_3 films were deposited onto glass substrates and SiO_2/Si substrates via RPD (Sumitomo Heavy Industries, URT-IP2).^[69] We used ceramic tablets (Sumitomo Metal Mining) with different impurities: pure In_2O_3 , In_2O_3 with a WO_3 content of 1 wt.%, and In_2O_3 with CeO_2 contents of 1, 2, and 3 wt.%. The deposition gases were Ar, O_2 , and H_2O at a total pressure of ≈ 0.4 Pa. The flow ratio of O_2 to Ar was fixed at 24%, whereas the $P_{\text{H}_2\text{O}}$ was varied from 1×10^{-5} to 5×10^{-4} Pa before deposition monitored by quadrupole mass spectrometry (Inficon, Transpector XPR3). For the fabrication of the *poly*- In_2O_3 , $\text{In}_2\text{O}_3:\text{W}$, and $\text{In}_2\text{O}_3:\text{Ce}$ films, the films were deposited at 200°C . Here, we used the notation without H because the heated substrate and growth surface suppressed the incorporation of a large amount of hydrogen into the film, as described in Section 2.1. However, the *a*- $\text{In}_2\text{O}_3:\text{H}$, $\text{In}_2\text{O}_3:\text{W,H}$, and $\text{In}_2\text{O}_3:\text{Ce,H}$ films were fabricated without intentional substrate heating. The maximum substrate temperatures were observed to be less than 60°C during deposition using thermolabels attached to the glass and SiO_2/Si substrates. After deposition, some films were post-annealed at 250°C under vacuum to obtain crystallized films.

Most of the characterizations of the films were conducted using 220-nm-thick films on glass. Hereafter, we describe the layer structure when the characterization was conducted using specimens other than 220-nm-thick films on glass. The hydrogen contents in the films were evaluated by HFS (CEA) and TDS (ESCO, EMD-1000S) using 220-nm-thick films on SiO_2/Si substrates. The contents of metal impurities within the films were analyzed using ICP-MS (Agilent, 8900 ICP-QQQ). The surface morphology and crystallinity of the films were analyzed by SEM (Hitachi, S-4300) and XRD (Rigaku, SmartLab), respectively. EBSD (JEOL, JSM-7001F) was used to evaluate the crystalline orientation of each grain at an electron acceleration voltage of 15 keV. The ρ , N , and μ values of the films were determined from Hall measurements (Toyo, ResiTest8300) in van der Pauw configurations at room temperature. The temperature dependence of the electrical properties was also evaluated every 10°C from 40 to 250°C , with subsequent cooling from 250°C to room temperature. During heating, the films crystallized. The optical constants of the films were determined by SE (J. A. Woolam, M-2000) using 60-nm-thick films on SiO_2/Si substrates. Here, the optical constants at each wavelength were mathematically derived by inverting the measured SE

spectra using the Fresnel equations. The details of this procedure have been described elsewhere.^[47]

Acknowledgments

This work was supported by the National Institute of Advanced Industrial Science and Technology (AIST) and the New Energy and Industrial Technology Development Organization (NEDO) under the Ministry of Economy, Trade and Industry (METI), Japan.

Conflict of Interest

The authors declare no conflict of interest.

Keywords

doping, indium oxide, mobility, solid-phase crystallization, transparent conducting oxide

Received: July 20, 2017

Revised: January 17, 2018

Published online:

- [1] A. E. Delahoy, S. Y. Guo, *J. Vac. Sci. Technol. A* **2005**, 23, 1215.
- [2] J. A. A. Slevan, A. E. Delahoy, S. Guo, Y. Li, *Sol. Energy Mater. Sol. Cells* **2006**, 90, 3371.
- [3] T. Koida, H. Fujiwara, M. Kondo, *Appl. Phys. Express* **2008**, 1, 041501.
- [4] M. Taguchi, A. Yano, S. Tohoda, K. Matsuyama, Y. Nakamura, T. Nishiwaki, K. Fujita, E. Maruyama, *IEEE J. Photovolt.* **2014**, 4, 96.
- [5] F. Meng, J. Shi, Z. Liu, Y. Cui, Z. Lu, Z. Feng, *Sol. Energy Mater. Sol. Cells* **2014**, 122, 70.
- [6] E. Kobayashi, Y. Watabe, T. Yamamoto, Y. Yamada, *Sol. Energy Mater. Sol. Cells* **2016**, 149, 75.
- [7] J. Meier, J. Spitznagel, U. Kroll, C. Bucher, S. Fay, T. Moriaty, A. Shah, *Thin Solid Films* **2004**, 451–452, 518.
- [8] S. Fay, U. Kroll, C. Bucher, E. Vallat-Sauvain, A. Shah, *Sol. Energy Mater. Sol. Cells* **2005**, 86, 385.
- [9] O. Kluth, B. Rech, L. Houben, S. Wieder, G. Schope, C. Beneking, H. Wagner, A. Löffl, H. W. Schock, *Thin Solid Films* **1999**, 351, 247.
- [10] M. Berginski, J. Huples, M. Schulte, G. Schope, H. Stiebig, B. Rech, M. Wuttig, *J. Appl. Phys.* **2007**, 101, 074903.
- [11] K. Sato, Y. Gotoh, Y. Hayashi, K. Adach, H. Nishimura, Reports Res. Laboratory Asahi Glass Co. Ltd. **1990**, 40, 233.
- [12] T. J. Coutts, D. L. Young, X. Li, *MRS Bull.* **2000**, 25, 58.
- [13] T. J. Coutts, D. L. Young, T. A. Gessert, in *Handbook of Transparent Conductors* (Eds: D. Ginley, H. Hosono, D. C. Paine), Springer, New York **2010**, Ch. 3, pp. 51–110.
- [14] A. E. Delahoy, S. Guo, in *Handbook of Photovoltaic Science and Engineering*, 2nd ed. (Eds: A. Luque, S. Hegedus), Wiley, Chichester **2011**, Ch. 17, pp. 716–796.
- [15] T. Koida, *Phys. Stat. Solidi (a)* **2017**, 214, 1600464.
- [16] M. Morales-Masis, S. De Wolf, R. Woods-Robinson, J. W. Ager, C. Ballif, *Adv. Electron. Mater.* **2017**, 3, 1600529.
- [17] S. De Wolf, M. Kondo, *J. Appl. Phys.* **2009**, 105, 103707.
- [18] M. Morales-Masis, S. M. De Nicolas, J. Holovsky, S. De Wolf, C. Ballif, *IEEE J. Photovolt.* **2015**, 5, 1340.
- [19] J. Guillemoles, L. Kronik, D. Cahen, U. Rau, A. Jasenek, H. W. Schock, *J. Phys. Chem. B* **2000**, 104, 4849.
- [20] S. Kijima, T. Nakada, *Appl. Phys. Express* **2008**, 1, 075002.
- [21] A. Dualeh, N. Tetreault, T. Moehl, P. Gao, M. K. Nazeeruddin, M. Gratzel, *Adv. Funct. Mater.* **2014**, 24, 3250.
- [22] J. Werner, G. Dubuis, A. Walter, P. Löper, S. Moon, S. Nicolay, M. Morales-Masis, S. De Wolf, B. Niesen, C. Ballif, *Sol. Energy Mater. Sol. Cells* **2015**, 141, 407.
- [23] G. Frank, H. Kostlin, *Appl. Phys. A: Solids Surf.* **1982**, 27, 197.
- [24] I. Hamberg, C. G. Granqvist, *J. Appl. Phys.* **1986**, 60, R123.
- [25] R. F. Dhere, T. A. Gessert, L. L. Schilling, A. J. Nelson, K. M. Jones, A. Aharoni, T. J. Coutts, *Solar Cells* **1987**, 21, 281.
- [26] S. Ishibashi, Y. Highchi, Y. Ota, K. Nakamura, *J. Vac. Sci. Technol. A* **1990**, 8, 1403.
- [27] T. Minami, T. Kakumu, S. Takata, *J. Vac. Sci. Technol. A* **1996**, 14, 1704.
- [28] A. Kaijo, K. Inoue, S. Matsuzaki, Y. Shigesato, in *PRICM 4: Forth Pacific Rim International Conference on Advanced Materials and Processing*, Vols. 1 and 2. **2001**, p. 1787.
- [29] Y. Shigesato, S. Takaki, T. Haranoh, *J. Appl. Phys.* **1992**, 71, 3356.
- [30] R. Martins, P. Barquinha, A. Pimentel, L. Pereira, E. Fortunato, *Phys. Status Solidi A* **2005**, 202, R95.
- [31] A. J. Leenheer, J. D. Perkins, M. F. A. M. van Hest, J. J. Berry, R. P. O'Hayre, D. S. Ginley, *Phys. Rev. B* **2008**, 77, 115215.
- [32] M. F. A. M. van Hest, M. S. Dabney, J. D. Perkins, D. S. Ginley, M. P. Taylor, *Appl. Phys. Lett.* **2005**, 87, 032111.
- [33] T. Asikainen, M. Ritala, M. Leskela, *Thin Solid Films* **2003**, 440, 152.
- [34] T. Koida, M. Kondo, *J. Appl. Phys.* **2007**, 101, 063713.
- [35] Y. Meng, X. Yang, H. Chen, J. Shen, Y. Jiang, Z. Zhang, Z. Hua, *Thin Solid Films* **2001**, 394, 219.
- [36] Y. Meng, X. Yang, H. Chen, J. Shen, Y. Jiang, Z. Zhang, Z. Hua, *J. Vac. Sci. Technol. A* **2002**, 20, 288.
- [37] Y. Yoshida, T. A. Gessert, C. L. Perkins, T. J. Coutts, *J. Vac. Sci. Technol. A* **2003**, 21, 1092.
- [38] Y. Yoshida, D. M. Wood, T. A. Gessert, T. J. Coutts, *Appl. Phys. Lett.* **2004**, 84, 4.
- [39] C. Warmingsingh, Y. Yoshida, D. W. Readey, C. W. Teplin, J. D. Perkins, P. A. Parilla, L. M. Gedvilas, B. M. Keyes, D. S. Ginley, *J. Appl. Phys.* **2004**, 95, 3831.
- [40] P. F. Newhouse, C.-H. Park, D. A. Keszler, J. Tate, P. S. Nyholm, *Appl. Phys. Lett.* **2005**, 87, 112108.
- [41] T. Koida, H. Fujiwara, M. Kondo, *Jpn. J. Appl. Phys.* **2007**, 28, L685.
- [42] E. Kobayashi, Y. Watabe, T. Yamamoto, *Appl. Phys. Express* **2015**, 8, 015505.
- [43] B. Maccio, Y. Wu, D. Vanhemel, W. M. M. Kessels, *Phys. Status Solidi RRL* **2014**, 8, 987.
- [44] T. Koida, M. Kondo, *J. Appl. Phys.* **2007**, 101, 063705.
- [45] T. Koida, H. Fujiwara, M. Kondo, *J. Non-Cryst. Solids* **2008**, 354, 2805.
- [46] H. Fujiwara, M. Kondo, *Phys. Rev. B* **2005**, 71, 075109.
- [47] T. Koida, M. Kondo, K. Tsutsumi, A. Sakaguchi, M. Suzuki, H. Fujiwara, *J. Appl. Phys.* **2010**, 107, 033514.
- [48] O. Lozano, Q. Y. Chen, P. V. Wadekar, H. W. Seo, P. V. Chinta, L. H. Chu, L. W. Tu, I. Lo, S. W. Yeh, N. J. Ho, F. C. Chuang, D. J. Jang, D. Wijesundera, W.-K. Chu, *Sol. Energy Mater. Sol. Cells* **2013**, 113, 171.
- [49] N. Preissler, O. Bierwagen, A. T. Ramu, J. S. Speck, *Phys. Rev. B* **2013**, 88, 085305.
- [50] M. Feneberg, J. Nixdorf, C. Lidig, R. Goldhahn, Z. Galazka, O. Bierwagen, J. S. Speck, *Phys. Rev. B* **2016**, 93, 045203.
- [51] J. W. Orton, M. J. Powell, *Rep. Prog. Phys.* **1980**, 43, 81.
- [52] K. Ellmer, R. Mientus, *Thin Solid Films* **2008**, 516, 4620.
- [53] M. V. Frischbier, H. F. Wardenga, M. Weidner, O. Bierwagen, J. Jia, Y. Shigesato, A. Klein, *Thin Solid Films* **2016**, 614, 62.
- [54] S. Calnan, A. N. Tiwari, *Thin Solid Films* **2010**, 518, 1839.
- [55] S. Limpijumng, P. Reunchan, A. Janotti, C. G. Van de Walle, *Phys. Rev. B* **2009**, 80, 193202.
- [56] J. B. Varley, H. Peelaers, A. Janotti, C. G. Van de Walle, *J. Phys.: Condens. Matter* **2011**, 23, 334212.

- [57] B. Macco, H. C. M. Knoop, W. M. M. Kessels, *ACS Appl. Mater. Interfaces* **2015**, 7, 16723.
- [58] A. Walsh, C. R. A. Catlow, *J. Mater. Chem.* **2010**, 20, 10438.
- [59] J. E. Medvedeva, D. B. Buchholz, R. P. H. Chang, *Adv. Electron. Mater.* **2017**, 3, 1700082.
- [60] H. Kitami, M. Miyashita, T. Sakemi, Y. Aoki, T. Kato, *Jpn. J. Appl. Phys.* **2015**, 54, 01AB05.
- [61] T. Kamiya, K. Nomura, M. Hirano, H. Hosono, *Phys. Stat. Solidi (a)* **2009**, 206, 860.
- [62] T. Koida, H. Sai, H. Shibata, M. Kondo, *Jpn. J. Appl. Phys.* **2014**, 53, 05FA08.
- [63] R. L. Weiher, R. P. Ley, *J. Appl. Phys.* **1966**, 37, 299.
- [64] A. Walsh, J. L. F. Da Silva, S.-H. Wei, C. Korber, A. Klein, L. F. J. Piper, A. DeMasi, K. E. Smith, G. Panaccione, P. Torelli, D. J. Payne, A. Bourlange, R. G. Egdell, *Phys. Rev. Lett.* **2008**, 100, 167402.
- [65] F. Fuchs, F. Bechstedt, *Phys. Rev. B* **2008**, 77, 155107.
- [66] P. D. C. King, T. D. Veal, F. Fuchs, Ch. Y. Wang, D. J. Payne, A. Bourlange, H. Zhang, G. R. Bell, V. Cimalla, O. Am-bacher, R. G. Egdell, F. Bechstedt, C. F. McConville, *Phys. Rev. B* **2009**, 79, 205211.
- [67] K. Irmscher, M. Naumann, M. Pietsch, Z. Galazka, R. Uecker, T. Schulz, R. Schewski, M. Albrecht, R. Fornari, *Phys. Status Solidi Appl. Mater. Sci.* **2014**, 211, 54.
- [68] J. E. Medvedeva, *Phys. Rev. Lett.* **2006**, 97, 086401.
- [69] K. Iwata, T. Sakemi, A. Yamada, P. Fons, K. Awai, T. Yamamoto, S. Shirakata, K. Matsubara, H. Tampo, K. Sakurai, S. Ishizuka, S. Niki, *Thin Solid Films* **2005**, 480–481, 199.